

# Multi-Calorimetry in Light-based Neutrino Detectors

Anatael Cabrera<sup>\*1,2,3</sup>, Yang Han<sup>†4,1,2</sup>, Steven Calvez<sup>5</sup>, Emmanuel Chauveau<sup>6</sup>, Hanyi Chen<sup>1</sup>, Hervé de Kerret<sup>‡2</sup>, Stefano Dusini<sup>7</sup>, Marco Grassi<sup>8</sup>, Leonard Imbert<sup>5</sup>, Jiajun Li<sup>4</sup>, Roberto Carlos Mandujano<sup>9</sup>, Diana Navas-Nicolás<sup>1</sup>, Hiroshi Nunokawa<sup>10,1</sup>, Michel Obolensky<sup>2</sup>, Juan Pedro Ochoa-Ricoux<sup>9</sup>, Guillaume Pronost<sup>11,5</sup>, Benoit Viaud<sup>5</sup>, and Frederic Yermia<sup>5</sup>

<sup>1</sup>Université Paris-Saclay, CNRS/IN2P3, IJCLab, Orsay, France

<sup>2</sup>Université de Paris Cité, CNRS, APC, Paris, France

<sup>3</sup>LNCA Underground Laboratory, CNRS, EDF Chooz Nuclear Reactor, Chooz, France

<sup>4</sup>Sun Yat-sen University, Guangzhou, China

<sup>5</sup>Nantes Université, IMT-Atlantique, CNRS/IN2P3, Subatech, Nantes, France

<sup>6</sup>Université de Bordeaux, CNRS, LP2I Bordeaux, Gradignan, France

<sup>7</sup>INFN, Sezione di Padova, Padova, Italy

<sup>8</sup>Dipartimento di Fisica e Astronomia dell'Università di Padova and INFN Sezione di Padova, Padova, Italy

<sup>9</sup>Department of Physics and Astronomy, University of California at Irvine, Irvine, CA, USA

<sup>10</sup>Department of Physics, Pontificia Universidade Católica do Rio de Janeiro, Rio de Janeiro, Brazil

<sup>11</sup>ILANCE, CNRS - University of Tokyo International Research Laboratory, Kashiwa, Chiba, Japan

Neutrino detectors are among the largest photonics instruments built for fundamental research. Since its inception, neutrino detection has been inexorably linked to the challenging detection of scarce photons in huge instrumented volumes. Many discoveries in neutrino physics, including the neutrino itself, are inseparable from the evolution of the detector photonics interfaces, i.e. photo-sensors and readout electronics, to yield ever higher precision and richer detection information. The measurement of the energy of neutrinos, referred to as *calorimetry*, is pursued today to reach permille level systematics control precision, thus leading to further innovation in specialised photonics. This publication describes a novel articulation that detectors may be endowed with multiple photonics interfaces for simultaneous light detection to yield unprecedented high-precision calorimetry. This *multi-calorimetry* approach opens the novel notion of *dual-calorimetry* detectors as an evolution from the *single-calorimetry* setups used over several decades for most experiments so far. The dual-calorimetry design exploits unique response synergies between photon-counting and photon-integration detection systems, including correlations and cancellations between calorimetric responses, to yield the unprecedented mitigation of the dominant response systematic effects today for the possible improved design of a new generation of neutrino experiments.

Neutrino detectors are amongst the largest high-precision photonics systems. Photons, produced via rare neutrino interactions in light-based detectors, travel quasi-unimpededly over long distances across transparent monolithic media, and then, they can be detected by photo-sensors. This is the basis of one of the most successful workhorse technologies, leading to many neutrino-related discoveries over several decades, as evidenced by several Nobel prizes [1, 2, 3]. The art of neutrino detection is tightly linked to advances in photon detection, and it is expected to remain so for the foreseeable future. Thanks to their sizeable photosensitive area per channel (up to  $\sim 0.2\text{ m}^2$ ), the most common photo-sensor remains the photo-multiplier tube (PMT), invented in the 1930s [4].

The main challenge of neutrino detectors stems from their monumental size, needed to compensate for the tiny neutrino detection probability, so the detection of photons takes place over distances of up to a hundred meters across. Indeed, neutrino detection is likely one of the most intrepid achievements in particle physics. These particles are known for their ability to traverse matter, including our planet, with little attenuation. Remarkably, most neutrino detection reduces to light detection with photonics instruments; meanwhile, the detection systematics control is crucial to achieve high-precision measurement. However, one of the most challenging applications of these photonics instruments is that the specific photon detection solution remains primarily constrained by the detector dimension and corre-

\*Contact: anatael@in2p3.fr

†Contact: hany88@mail.sysu.edu.cn

‡Deceased

sponding cost-effective compromises while pursuing high precision. A novel light detection technique, called *dual-calorimetry*, is explored and tailored to excel within these constraints, which is the main subject of this publication.

Within today’s neutrino detectors, the pioneering *liquid scintillator detector* (LSD) has been the most widely used. Scintillating materials as the detector medium enable the detection of additional light [5] relative to the irreducible Cherenkov radiation [6, 7], both emitted by charged particles generated upon neutrino interactions. Therefore with about one hundred times more light, higher energy resolution at the level of several percent in the MeV scale and lower energy detection threshold, e.g. tens of keV, are possible in LSD [8]. Instead, when using only Cherenkov light, the energy threshold is typically a few MeV [9, 10]. A general view of the light-based neutrino LSD is described in Figure 1.a, in which the detection medium is a monolithic liquid scintillator (LS) and the photonics interface typically consists of photo-sensors and readout electronics.

The LSD technology has led to major fundamental neutrino discoveries and measurements. Those achievements include the neutrino discovery [11], the first reactor neutrino oscillation studies and measurements by the Chooz [12], Palo Verde [13] and KamLAND [14], the first accelerator-based neutrino oscillation studies by LSND [15] and KARMEN [16], the discovery of the Earth’s radioactivity geoneutrino by KamLAND [17], the first observation of the model-predicted third-neutrino-oscillation by Daya Bay [18], Double Chooz [19] and RENO [20], and the observation of all solar neutrino components by Borexino [21, 22, 23, 24, 25]. Most recently, even the world leading precision in neutrino-less double-beta decay searches benefits from these detectors, as demonstrated by the KamLAND-Zen [26], and soon also SNO+ [27].

Detectors based only on Cherenkov radiation hold a similar photonics interface as LSD. Larger volumes for water Cherenkov detectors are possible by the absence of scintillators due to the higher transparency in water but at the expense of scarcer light for detection. The discovery of neutrino oscillations led by Super-Kamiokande [28], the largest-built detector so far ( $\sim 5 \times 10^4 \text{ m}^3$ ), and SNO [29], as well as the first observation of neutrinos from a supernova core-collapse explosion by the Kamiokande [30] and IMB [31] experiments, rejoin this photonics technology *palmarès*. Scaling up the same rationale, Hyper-Kamiokande [32] detector, under construction, is reaching the unprecedented instrumented volume of  $\sim 2.5 \times 10^5 \text{ m}^3$ . While using the natural existing detection medium, there are also

Antarctica’s ice [33], Mediterranean sea [34] and Baikal lake [35] *neutrino telescopes*, in the ongoing operation, with a total volume of order  $\sim 10^9 \text{ m}^3$ .

The next generation neutrino LSD may be represented by the JUNO experiment [8], also under construction, reaching the cutting-edge technology for the highest light detection precision with a huge detector size ( $\sim 2 \times 10^4 \text{ m}^3$ ). Its physics target imposes the calorimetry design to reach a vertiginous control of the energy systematics at the sub-percent level total budget over one of the vastest photon detection dynamic ranges. Indeed, the unprecedented requirement in a JUNO-like detector opened a new twist in the LSD photon detection innovation, leading to the conception of the novel *dual calorimetry*, first proposed in 2014, released later on [36, 37] and here described for the first time. Some of its fundamental elements were pre-conceived in the energy control strategy of Double Chooz [38].

The notion of dual-calorimetry described here aims at the robust light detection via the redefinition of the photonics interface for the most stringent systematics control. Indeed, the dual-calorimetry relies on two synergetic and complementary photonics interfaces in one detector and can be considered as an evolution from the *single calorimetry* basis, i.e. single photonics interface used by most light-based neutrino detectors so far. From a different perspective, dual-calorimetry could instead exploit other physics complementary observables different from light. Excellent examples exist when scintillation light (i.e. photons) are combined with heat, in the context of scintillating bolometers [39], or with the disassociated electrons in noble liquid (or gases) TPC-detectors [40]. However, the rest of our discussion shall focus on photonics-only dual-calorimetry .

## Calorimetry in LSD

The notion of *calorimetry* implies the measurement of *energy*. The calorimetry in LSD is realised by measuring the light yielded upon the interaction of particles in the scintillator, which is feasible due to the intrinsic transducer ability of the scintillator to convert the deposited energy into light while following a monotonic proportionality relation. The energy estimated by light is referred to as *visible energy*, as opposed to the *neutrino energy*, which may only be inferred a posteriori from visible energy. The *visible energy* will be referred to as *energy* from now on, and it is the main photonics observable of monolithic transparent LSDs. In addition, by using the time-of-flight triangulation and/or the distribution of detected photons across photo-sensors, LSD can infer the *vertex* position per energy deposition.

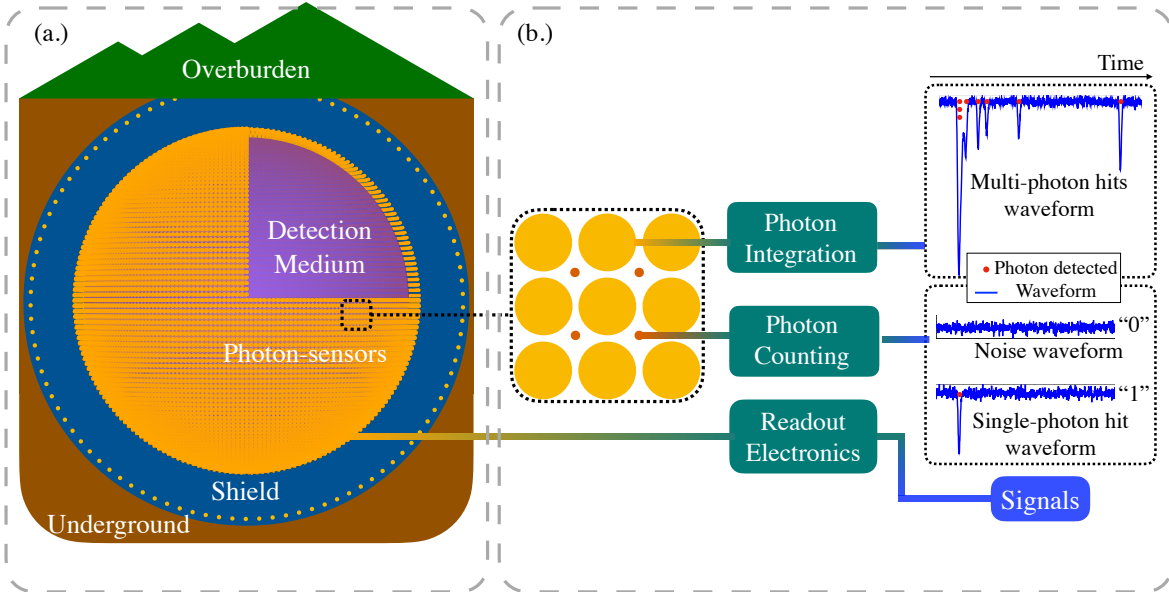


Figure 1: **(a.) Light-based Neutrino LSD Typical Configuration.** A neutrino detector is typically underground and equipped with shielding systems for environmental background reduction. The detection system consists of a detection medium (purple), e.g. liquid scintillator, surrounded by photo-sensors (orange) whose signals (blue) are read out through electronics. **(b.) Dual Calorimetry Configuration.** Single photo-sensor (SPS) with large surface can receive multi-photon hits, thus requiring its electronics to sample the signal pulse waveform and integrate it over time, i.e. photon-integration. As long as the SPS is small enough such that single-photon hits dominate, it can be sufficient for its electronics to keep minimal functionality to discriminate single-photon from noise, i.e. photon-counting. The dual-calorimetry enables both photon-integration and photon-counting calorimeters in a single LSD by having two sets of photo-sensors around the common detection volume.

However, light-derived information in monolithic transparent LSD is known to have limitations in revealing event-by-event information, such as event topology, directionality and particle identification, despite advanced analysis techniques such as pulse-shape discrimination [41]. Modifying the detector design could overcome some of those limitations. The adoption of the opacity in LSD is expected to enable event topology from MeV energies, as pioneered by LiquidO [42]. Event-by-event information may also be resolved by segmenting the LSD as done in NOvA for GeV energies [43], as well as by using segmented solid scintillators, e.g. MINOS [44], T2K-ND280 [45], Solid [46] and DANSS [47]. Enhancing the exploitation of Cherenkov light is expected to provide event directionality as recently shown [48, 49]. This may be further enhanced by adopting specialised formulations of liquid scintillators, such as water-based scintillators [50, 51, 52] and slow scintillators [53, 54]. While complementary, the energy control of non-monolithic scintillator detectors can be significantly different, so its specifics are not covered below.

Sticking to the major calorimetric measurements in monolithic LSD, the focuses are energy scale and resolution. The energy scale specifies the conversion relation

from the detected photons to the deposited energy, and its precision is driven by calorimetric response systematics. The energy resolution specifies the stochastic and non-stochastic fluctuations of detected photons given a certain energy deposition. The inherent stochastic Poisson fluctuation is driven by the photon statistics, while the aggregate of all non-stochastic terms is caused by systematic effects of calorimetric response.

Regarding the calorimetric response ( $R$ ), there are three general types of effects affecting its systematics. Those are (i) *non-linearity* (NL), (ii) *non-stability* (NS), and (iii) *non-uniformity* (NU), which are, respectively, the manifestation of deviations in the detected light output from a perfectly linear response to energy, a constant response in time, and a uniform response across the detection volume. These effects are often unavoidable aspects within the LSD photonics processes due to inaccuracies in their control, thus affecting the characterisation of the energy scale and resolution.

There are known deviations from linearity in the scintillator response since there are particle-dependent excitation-quenching effects at low energies [5]. Moreover, in an oil-based scintillator, the Cherenkov radiation has a production threshold of around 0.2 MeV for electrons. The above effects bias the response from lin-

earity while having understood physics reasons. However, leading-order instrumentation effects can cause additional complex non-linearities during the inclusive photon detection processes at the stages of photo-sensors, readout electronics, reconstruction, as well as their interfaces. Both physical and instrumental non-linearity effects lead to an effective interlaced nonlinear response, where the former originates at the generation of detectable light, and the latter can be regarded as a consequence of the conversion of detected light into readout *charge*. Time-wise non-stabilities are induced typically by detector-wise changes in time with temperature, detection medium evolution, and readout configuration changes during the lifetime of experiments. The non-uniformity effect is the manifestation of the non-uniform light collection across the detector primarily due to solid-angle acceptance so that the collected light with the same energy becomes detector position-dependent. This is expected to be corrected by using the calibration samples with known vertex position and energy.

More challengingly, realistic, complex scenarios arise upon the combination of NL, NS and NU effects, in which all effects are entangled in the overall measured calorimetric response. This, in turn, may translate into response degeneracies and biasing correlations in the overall measured energy, as will be illustrated later. Worse, some of those effects may not be corrected through conventional energy calibration schemes. This is due to limited calibration sampling of the light response across the combined linearity, time and position parameter space during the lifetime of the experiment. The implication of these limitations to the control of energy precision can be significant and is the motivation of the novel dual-calorimetry articulation, as will be discussed in detail later.

## Single Calorimetry LSD

Depending on the photonics technology employed, the observable of a single photo-sensor (SPS), i.e. the number of photons detected per channel ( $n_{pd}$ ), can be estimated in two distinct regimes here referred to as *photon-counting regime* (PCR) and *photon-integration regime* (PIR). The sum of the channel-wise  $n_{pd}$  yields the total number of photons detected across the entire detector ( $N_{pd}$ ), which is proportional to the event energy. Single calorimetry LSD is characterised by having a single-type photonics interface, typically sticking to either regime. It is worth highlighting that the systematics affecting each regime can be significantly different. As detailed below, the impact of systematics can indeed become the leading criterion for an experiment to opt for different

choices of photonics interface to attain its scientific goals given the required energy accuracy and precision.

The PCR occurs when single-photon detection is dominant. This implies opting for a photonics technology leading to the direct measurement, as opposed to inferred, of discrete detected single-photon. In this context, there may be little or even no need for charge digitisation, as a simple discriminator may enable a perfectly digital (i.e. “0” and “1”) readout per single detected photon; hence the photon ( $n_{pd}$ ) dynamic range is virtually zero, as shown in Figure 1.b. The calorimetry in PCR features a direct  $N_{pd}$  observable, immune to the charge measurement and its possible bias, Hence, it has a minimal systematic effect, i.e. the discrimination of single-photon from noise, leading promisingly to the robustness of the light detection.

When the pile-up of multiple photons per SPS is not negligible, the detection enters into the PIR, and light is effectively sampled and integrated as the integral charge over a certain time window, as highlighted in Figure 1.b. Thus, PIR defaults into photonics instrumentation, not easily allowing discrete single-photon information. In PIR, the photon detection exhibits a dynamic range driven by the energy range of detected events and the acceptance solid-angle of each photo-sensor. Since  $n_{pd}$  is indirectly derived, this method heavily depends on the photon-to-charge conversion, typically referred to as *gain*. The inferred  $n_{pd}$  is a priori sensitive to numerous systematic effects, such as photo-sensor gain non-linearity, signal pulse fluctuation and distortion, electronics noise, cross-talk among channels, charge reconstruction algorithm, etc. Moreover, the manifestation and impact of those effects would intensify with the increase of photon dynamic range.

Given a detector configuration, the leading order discriminator between PCR and PIR can be the photo-sensor dimension, as described in Figure 2. PIR is typically mandatory when the overall light level per readout channel is high. This means that the simplest way to implement PCR is to reduce the SPS detection surface so that the single-photon detection is dominant, covering variations over the entire targeted range in energy and volume. In order to reach the same total photo-sensitive area, the PCR using a small pixel, implies a more significant number of independent readout channels. More readout channels have typically led to a higher cost because, traditionally, the overall cost had decreased with maximal photocathode area per channel. Moreover, there is a non-negligible cost of logistical overheads, such as cabling, etc. This remains largely true still today, although dedicated solutions such as multiplexing, multi-channel readout ASICs, or even un-

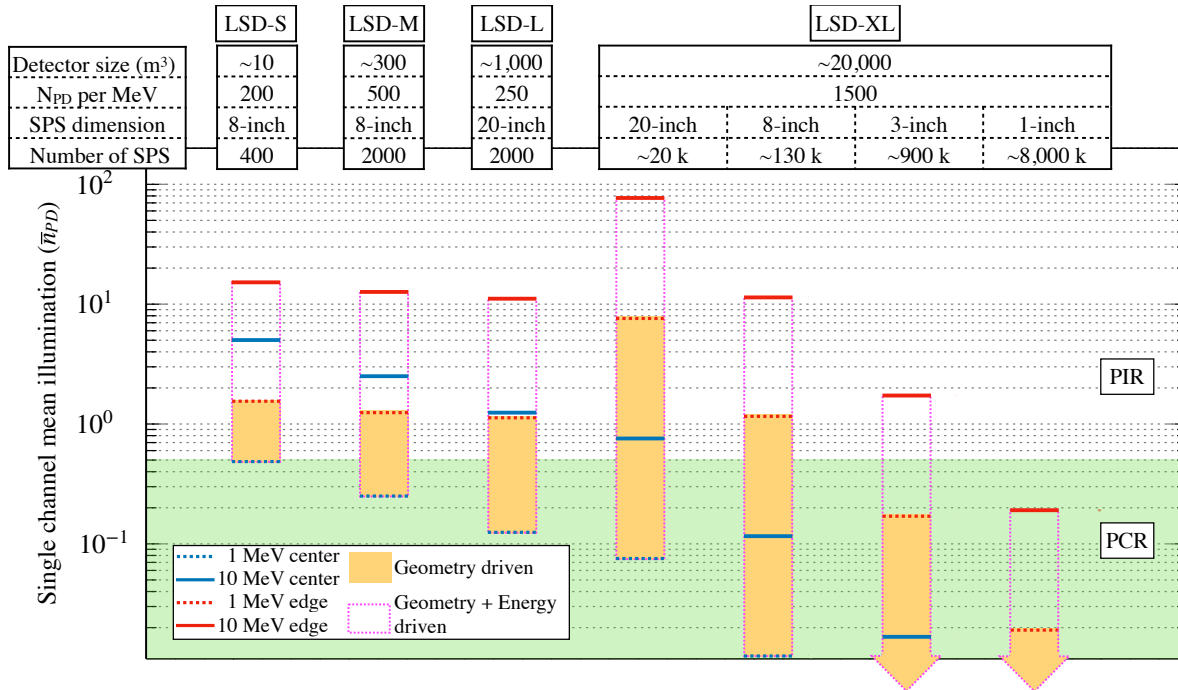


Figure 2: **Calorimetry Light Detection Regimes Illustration.** The light regime depends on the single channel mean illumination ( $\bar{n}_{PD}$ ). This is shown for four hypothetical detector configurations with different detector sizes: LSD-S (small), LSD-M (medium), LSD-L (large) and LSD-XL (extra-large), which can be considered as DoubleChooz-like, Borexino-like, KamLAND-like and JUNO-like detectors, respectively. The  $\bar{n}_{PD}$  is estimated based on simplified detector configurations by considering mainly the detector size, total photon detected ( $N_{DP}$ ) per MeV, SPS dimension and number of SPS. For each detector configuration, the  $\bar{n}_{PD}$  is calculated for I.) 1 MeV energy deposition at detector centre (dotted blue lines), II.) 10 MeV energy deposition at detector centre (solid blue lines), III.) 1 MeV energy deposition at detector edge (dotted red lines), IV.) 10 MeV energy deposition at detector edge (solid red lines). The yellow area represents the  $\bar{n}_{PD}$  range driven by detector geometry. The area surrounded by dotted magenta lines represents the  $\bar{n}_{PD}$  range driven by both the detector geometry and the energy range. The  $\bar{n}_{PD}$  of 0.5 PE is approximately considered as the bound between PCR and PIR. While the notion of photon dynamic range only makes sense for  $\bar{n}_{PD}$  above 0.5 PE, it is considered to be effectively zero for  $\bar{n}_{PD}$  below 0.5 PE. Only LSD-XL with 3-inch or 1-inch SPS configurations is predominantly in PCR, while the other configurations are mainly in PIR, as in most experiments so far. The LSD-XL with 20-inch SPS experiences the highest photon dynamic range. It should be noted that the number of SPS for LSD-XL detector is estimated for  $\sim 80\%$  total photosensitive coverage.

derwater readout deployment, thus minimising cabling, enable cost reduction at reasonable system reliability. Traditionally, the LSD design was mainly driven by the best cost-effective option. Consequently, PIR was the choice for most experiments in the past, as illustrated in Figure 2.

On the other hand, today’s latest signal waveform digitisation technology, such as FADC-based [55] or analogue-memory-based [56], provides the ability to mitigate the systematic effects associated with multi-photon detection, so that a PIR system may infer some of the information only native in PCR. A few neutrino experiments [57, 58] have fully adopted the waveform solutions, which even enable additional pulse-shape discrimination [59, 41, 60]. Waveform solutions are, however, not inexpensive, so the cost may favour a native PCR approach in suitable conditions. Moreover, waveform-derived solutions may suffer from the impact of non-negligible systematics due to reconstruction algorithms.

## Calorimetry Response Correlations

Given either PIR or PCR solution, the focus is the robustness of the control of energy systematics caused by unavoidable biases originating from the calorimetry response effects of NL, NS, and NU. In the ideal scenario of the perfect control of calorimetry systematics, PCR and PIR should lead to an effectively identical outcome. This necessitates one of the two conditions: a) the negligible native energy detection biases, or, b) the fact that all biases are perfectly corrected by an exhaustive calibration scheme. Unfortunately, this is rarely true in reality. In fact, it largely depends on the experiment-dependent calorimetry systematics tolerance for those biases to be effectively negligible – or not. While some experiments do physics within a few percent precision in the energy, the latest experiments targeting high-precision neutrino measurements are pushing the calorimetry systematics control to per-

mille level precision [61, 62], and more notably over an ever-vaster dynamic range [63], thus bringing to the foreground some bias effects that were negligible in the past. It is exactly in this context that the multi-calorimetry is conceived and expected to have its greatest impact.

To illustrate the impact of systematics, it is convenient to define the calorimetric response ( $R$ ) metric as

$$R = R_o \cdot \alpha_{NU} \cdot \alpha_{NS} \cdot \alpha_{NL}, \quad (1)$$

where  $R$  is characterised relative to a specific reference response  $R_o$ , and the normalised terms  $\alpha_i$  for NU, NS and NL will absorb the response dependencies on position ( $\vec{x}$ ), time ( $t$ ) and energy ( $E$ ), respectively. Subsequently, the response ( $R$ ), expressed in arbitrary units, provides the energy ( $E$ ), defined as

$$E = E_o \cdot \alpha_{NU} \cdot \alpha_{NS} \cdot \alpha_{NL}. \quad (2)$$

in energy units, such as MeV. Hence, the energy scale is a priori a function  $E(\vec{x}, t, R)$  and a constant  $E_o$  prior to calibration. The absolute calibration implies the relation  $E_o = \beta \cdot R_o$ , where  $\beta$  is the absolute energy conversion constant. The  $\alpha_i$  terms provide the relative realistic conversion of position, time and energy across the pertinent detector response dynamic range. Once perfectly calibrated, the effect of the  $\alpha_i$  is expected to be fully corrected so that the energy scale is linear, stable, and uniform across the detector.

Since, as mentioned before, the NL term has two different origins, physical and instrumental, linked to *light* ( $l$ ) and *charge* ( $q$ ), respectively, Equation 1 may be re-defined as

$$R = R_o \cdot \alpha_{NU} \cdot \alpha_{NS} \cdot [\alpha_{NL(l)} \otimes \alpha_{NL(q)}], \quad (3)$$

thus expressing, with the  $\otimes$ -sign, the entangled NL term as the combination of detector-wise light  $\alpha_{NL(l)}$  and channel-wise charge  $\alpha_{NL(q)}$  components, as if they were measured separately, which is in itself one of the challenges.

While some a priori information may exist about  $\alpha_{NL(l)}$  through measurements with test bench [64], the most faithful characterisation is done with the detector. More challengingly, it is difficult to directly access  $\alpha_{NL(q)}$  with the realistic detector configuration. This is a typical limitation of LSDs. And it is precisely for this reason that experiments relying on multi-detector configurations to yield inter-detector cancellation of response systematics have opted for the non-cost-effective use of several identical detectors, as originally proposed by Double Chooz [65], and successfully demonstrated for the entire field [66, 67].

In the presented response framework, there is a key assumption: each  $\alpha_i$  term is independent of one another, as suggested by the effective relation

$$\alpha_{NU} \otimes \alpha_{NS} \otimes \alpha_{NL} = 0, \quad (4)$$

where the  $\otimes$ -sign represents qualitatively the correlation, and zero means no correlation or *orthogonality*. This implies that each component can be measured and thus calibrated independently as if the response linearity, uniformity and stability bias effects were totally disjoint realms. This abstraction is, strictly speaking, not realistic, while it can be effectively acceptable if the impact of the correlations among those effects is small, which has been the case in most experiments so far. Again, the tolerance here depends on the ultimate energy scale precision envisioned by the experiment. The better the precision, the more important the correlation effects need to be considered; otherwise, non-negligible biases may arise. A key element is the channel-wise photon dynamic range, where the wider it is, the harder it will be to achieve precise energy control, as illustrated in Figure 3.a. So, experiments aiming for sub-percent energy precision and/or undergoing vast dynamic range are more susceptible to the complex response entanglements [38, 61, 63].

The response entanglement can be trivially illustrated with the  $\alpha_{NL}$  and  $\alpha_{NU}$  terms. As  $\alpha_{NU}$  is mainly driven by the solid angle per photo-sensor, the channel-wise detected photons  $n_{pd}$  varies as  $r^{-2}$ , where  $r$  is the distance between event position and photo-sensor. Therefore, scanning the response in position forcibly implies the simultaneous scan of  $n_{pd}$ , which is directly sensitive to  $\alpha_{NL(q)}$ . Hence, a genuine bias in linearity may manifest as an effective bias in uniformity, even if none really existed. This is illustrated with simulation as shown in Figure 4.a.II. If this were unknown, it would result in residual biases after calibration. It implies the need to modify the aforementioned response metric by adding the crossed-terms of the type  $\alpha_{ij}$ , leading to a hypothetical *response-tensor* representation. Therefore, one should measure and account for all the response correlations, which typically is experimentally impractical. Indeed, the inaccurate characterisation of the unavoidable response entanglement is a main limitation for high precision energy control today.

## Dual Calorimetry LSD

To overcome the response entanglement challenge, there are at least two possible solutions. One is to pursue an exhaustive calibration scheme to characterise the full response tensor, including all possible correlations. While

this may not be impossible, decades of experience reveal challenges due to limitations on calibration sources and deployments, e.g. limited available sources, positions and low calibration frequency across the lifetime of the detector. These limitations would largely impact the overall precision achievable by a given calibration scheme, which has been the main effort so far and should always remain the first consideration.

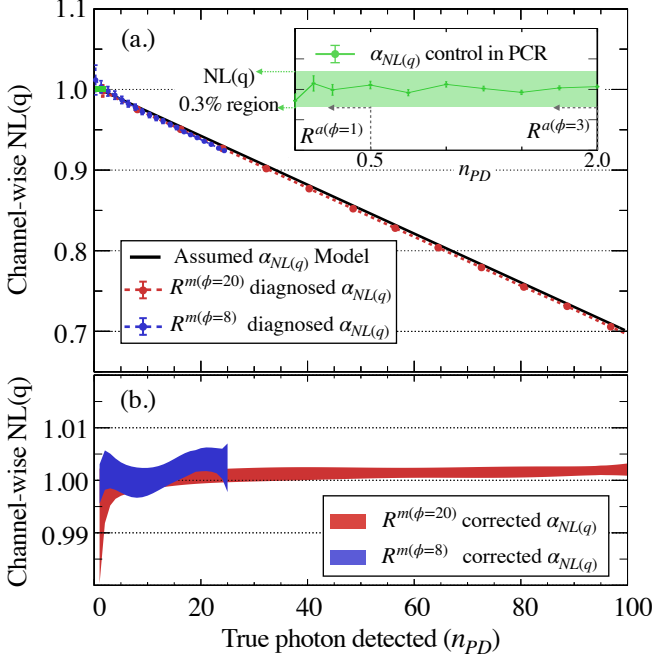


Figure 3: **(a.) Charge Non-linearity Illustration.** The channel-wise charge non-linearity  $\alpha_{NL(q)}$  is the ratio between the measured charge and true charge, here presented with the unit of  $n_{PD}$ . The LSD-XL configuration is used for illustration with a hypothetical  $\alpha_{NL(q)}$  model indicated by the black line. Given the same model, the SPS responses of 20-inch ( $R^{m(\phi=20)}$ ) and 8-inch  $R^{m(\phi=8)}$  undergo  $\sim 30\%$  and  $\sim 6\%$  NL(q) within their respective photon dynamic range. For the SPS responses of 3-inch ( $R^{(\phi=3)}$ ) and 1-inch ( $R^{(\phi=1)}$ ) with close to zero photon dynamic range, the linearity control can be achieved at permille level based on photon-counting [68]. **(b.) Charge Non-linearity Control Through Dual-Calorimetry.** With the *channel-wise dual-calorimetry calibration* approach, under  $C_{a(\phi=3 \text{ or } 1)}^{m(\phi=20)}$  and  $C_{a(\phi=3 \text{ or } 1)}^{m(\phi=8)}$  configurations, the  $\alpha_{NL(q)}$  in  $R^{(\phi=20)}$  and  $R^{(\phi=8)}$  can be diagnosed and then calibrated to permille level with the aid of the linear charge reference of  $R^{(\phi=3)}$  or  $R^{(\phi=1)}$ . Details are explained in the dual-calorimetry demonstration section.

The alternative is to innovate the detector design such that the impact of the inter-response correlations is essentially eliminated or significantly minimised. As the detector’s photonics system is the sole interface to the light response characterisation, the innovation is introduced here by adopting two independent photonics interfaces designed to operate in PIR and PCR, respec-

tively, inside one single detector, leading to the dual-calorimetry design as a minimal evolution from the traditional single-calorimetry in PIR. As detailed below, there exist synergy effects in the dual photonics interface, leading to the breakdown of the aforementioned response entanglements thanks to the cancellation of some key response terms. Therefore, the dual-calorimetry redefines the detector response basis where all  $\alpha_i$  terms can turn effectively orthogonal in the context of stringent response control and vast dynamic range conditions. This option can also be regarded as aiming to facilitate the calibration campaign and to spot possibly unforeseen systematics in light of obscure or unknown correlations.

While the best example today of dual-calorimetry design is JUNO, some of the key precursory building blocks and motivation of this approach were pioneered and exercised in the energy scale definition of Double Chooz, precisely to address its single-calorimetry design inherent limitations [38]. In Double Chooz, this was effectively done by defining and combining two single-calorimetry metrics, i.e. a PIR and an *ad hoc* PCR, from a single photonics interface, but it worked only in a very restricted low energy range at detector central area in order to fulfil the PCR condition. The dual-calorimetry introduced here explores a much richer synergy effect for the entire photon dynamic range and full detection volume thanks to enabling simultaneously two independent native PIR and PCR photonics interfaces.

## Dual Calorimetry formulation

By design, a dual calorimetry detector is endowed with two photonics systems, where the *main* system follows the generally more cost-effective PIR to collect most of the light, indicated by its response as

$$R^m = R_o^m \cdot \alpha_{NU}^m \cdot \alpha_{NS}^m \cdot [\alpha_{NL(l)}^m \otimes \alpha_{NL(q)}^m], \quad (5)$$

while a dedicated *auxiliary* system works in PCR with its response as

$$R^a = R_o^a \cdot \alpha_{NU}^a \cdot \alpha_{NS}^a \cdot [\alpha_{NL(l)}^a \otimes \alpha_{NL(q)}^a]. \quad (6)$$

Thanks to the effectively zero photon dynamic range of PCR thus charge immunity, it turns out  $\alpha_{NL(q)}^a \rightarrow 1$  in  $R^a$  and it becomes

$$R^a \approx R_o^a \cdot \alpha_{NU}^a \cdot \alpha_{NS}^a \cdot \alpha_{NL(l)}^a. \quad (7)$$

This way, the detector’s two photonics interfaces are like two disjoint detectors with a common receptacle. It is by design that the *main photonics interface* holds the main calorimetry estimator power, whose ultimate precision is being optimised. Instead, the *auxiliary photonics interface* collects less light over the same event samples.

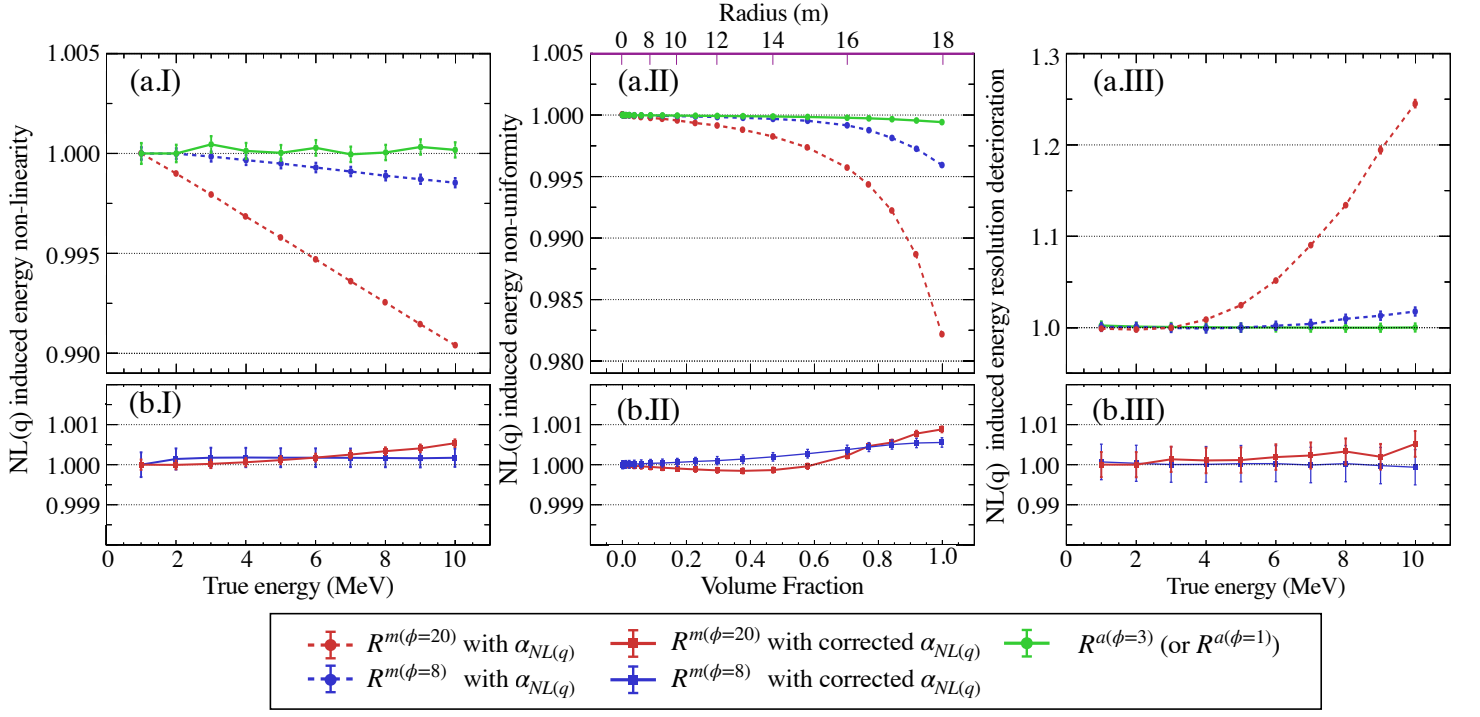


Figure 4: **(a.) Calorimetry Response Entanglement Illustration.** A hypothetical channel-wise  $NL(q)$  model is assumed to be the same as Figure 3.a. **(a.I)** The channel-wise  $NL(q)$  convolves into event-wise energy non-linearity with the events uniformly distributed in the full detection volume. **(a.II)** The position dependence of  $NL(q)$  makes it consequently entangling with NU, manifesting as a fake non-uniformity over a large fraction of detection volume, illustrated here with the events of 5 MeV energy. **(a.III)** The  $NL(q)$  could engender energy resolution deterioration due to biases in charge distribution and NU entanglement effect. The above biasing effects are more significant for  $R^{m(\phi=20)}$  and also sizeable for  $R^{m(\phi=8)}$ . While in  $R^{a(\phi=3)}$  or  $R^{a(\phi=1)}$  configurations, the response orthogonality can be ensured hence negligible response entanglement biasing effects. **(b.) Calorimetry Response Control through Dual-Calorimetry.** In  $C_{a(\phi=3 \text{ or } 1)}^{m(\phi=20)}$  and  $C_{a(\phi=3 \text{ or } 1)}^{m(\phi=8)}$  dual-calorimetry configurations, after the channel-wise calibration for  $NL(q)$  as demonstrated in Figure 3.b, the  $NL(q)$  induced energy NL bias, NU bias and energy resolution deterioration in PIR calorimetry (i.e.  $R^{m(\phi=20)}$  and  $R^{m(\phi=8)}$ ) can be restricted within permille level, shown in **(b.I)**, **(b.II)** and **(b.III)** respectively.

By construction, as both systems detect the same event, their calorimetry responses share some common, hence correlated, systematics including  $\alpha_{NL(l)}^a, \alpha_{NU}^a, \alpha_{NS}^a$ . Instead, the main-to-auxiliary photonics interfaces systematics (mainly  $\alpha_{NL(q)}^a$ ) are designed to be different, i.e. as uncorrelated as they can possibly be. Hence, the auxiliary PCR system's uncorrelated and robust information is used to enhance the calorimetry systematics control of the main system.

In dual-calorimetry, the common terms across the calorimetry responses of the  $R^m$  and  $R^a$  can be cancelled across a ratio by construction or upon optimisation if needed. Specifically, while comparing  $R^m$  and  $R^a$ , all common light generation effects (i.e.  $\alpha_{NL(l)}$ ) cancel, such as scintillation and Cherenkov radiation; the position-dependent effects (i.e.  $\alpha_{NU}$ ) fix to a constant given a static event vertex, and even though this constant varies with event vertex position, it can be calibrated; last, the commonality on  $\alpha_{NS}$  is due to the simultaneous detection of the same events in the common

detector medium, and frequent calibration could monitor the variation of detector response over time.

Considering all the above premises, the dual-calorimetry ratio is defined as

$$\frac{R^m}{R^a} = \frac{R_o^m \alpha_{NU}^m \cdot \alpha_{NS}^m \cdot [\alpha_{NL(l)}^m \otimes \alpha_{NL(q)}^m]}{R_o^a \alpha_{NU}^a \cdot \alpha_{NS}^a \cdot [\alpha_{NL(l)}^a]} \quad (8)$$

By cancelling the correlated terms, i.e.  $\alpha_{NU}^m/\alpha_{NU}^a \rightarrow 1$ ,  $\alpha_{NS}^m/\alpha_{NS}^a \rightarrow 1$  and  $\alpha_{NL(l)}^m/\alpha_{NL(l)}^a \rightarrow 1$ , the dual-calorimetry ratio transforms into

$$\frac{R^m}{R^a} = \frac{R_o^m}{R_o^a} \alpha_{NL(q)}^m, \quad (9)$$

where  $R_o^m$  and  $R_o^a$  are constant to be measured during calibration, thus isolating the behaviour of  $\alpha_{NL(q)}^m$ . Figure 3.a demonstrates the cancellation of all common responses and isolation of  $\alpha_{NL(q)}^m$ .

Expressed in terms of energy, this leads to

$$\frac{E^m}{E^a} = \frac{E_o^m}{E_o^a} \alpha_{NL(q)}^m = \alpha_{NL(q)}^m, \quad (10)$$



where  $E_o^m$  is equal to  $E_o^a$  as the absolute anchored energy. These two energies must be reconstructed identically across both readout interfaces regardless. Deviations can only be caused by possible systematic effects that can thus be measured modulo uncorrelated fluctuations (i.e. energy resolution).

Thus, the dual-calorimetry ratio can provide a clean and unbiased in-situ measurement of the otherwise elusive  $\alpha_{NL(q)}^m$ . This term has been proven one of the most challenging and dominant contributions to the latest best precision experiments (with  $O(10)$   $m^3$  detectors), where their control of energy scale was close to the  $\sim 0.5\%$  precision [38, 61].

Moreover, the dual-calorimetry opens a new handle for detector photonics interface optimisation, i.e. to maximise some  $\alpha_i$  commonalities across both systems, thus maximising cancellations over the parameter space and isolating the parameters of interest.

The orchestration of the dual-calorimetry with different calibration sources and systems can be especially powerful since this allows the exploitation of high activity and high luminosity calibration sources (i.e. high event statistics covering the entire photon dynamic range of interest within short periods), such as laser or LED light sources. By design, they can be deployed at a given time and favourably in the central detector region, so they may exploit, respectively, the cancellations  $\alpha_{NU}^m/\alpha_{NU}^a \rightarrow 1$  and  $\alpha_{NS}^m/\alpha_{NS}^a \rightarrow 1$ . Indeed, the scenario of a coherent dual-calorimetry-based calibration [68] offers the best context for a quantified demonstration, as shown next.

### Dual Calorimetry Demonstration

In order to demonstrate the dual-calorimetry, a Monte Carlo simulation-based analysis is performed with a hypothetical LSD detector design of the largest scale so far ( $\sim 2 \times 10^4$   $m^3$  volume), which can be considered as JUNO-like, as shown in Figure 1. The typical energy of interest of LSD in neutrino physics, i.e.  $1 \sim 10$  MeV, is targeted. This exercise aims to reach the energy scale control within permille level (up to the minimal 0.1%) deviation over a vast photon ( $n_{pd}$ ) dynamic range up to  $O(10^2)$ , shown as ‘‘LSD-XL’’ in Figure 2, for combined response variations due to linearity and uniformity.

To render the exercise more representative, the *main photonics interface* will rely on SPS of 20-inch diameter in PIR, which corresponds to the largest possible PMT available in the market [70, 71] and used by most of the large experiments now. Its response is referred to as  $R^{m(\phi=20)}$ . Similarly, the response of a hypothetical 8-inch SPS ( $R^{m(\phi=8)}$ ) is also considered to lead to a reduced dynamic range. As the *auxiliary photonics*

*interface*, two SPS of diameters 3-inch and 1-inch are considered to increasingly match the PCR condition, as indicated in Figure 2, whose respective responses will be noted as  $R^{a(\phi=3)}$  and  $R^{a(\phi=1)}$ .

Four configurations are considered to illustrate the dual-calorimetry principle and performance:

- I:**  $R^{m(\phi=20)}$  with  $\sim 15,000$  20-inch SPS and  $R^{a(\phi=3)}$  with  $\sim 50,000$  3-inch SPS, denoted as  $C_{a(\phi=3)}^{m(\phi=20)}$ .
- II:**  $R^{m(\phi=8)}$  with  $\sim 100,000$  8-inch SPS and  $R^{a(\phi=3)}$  with  $\sim 50,000$  3-inch SPS, denoted as  $C_{a(\phi=3)}^{m(\phi=8)}$ .
- III:**  $R^{m(\phi=20)}$  with  $\sim 15,000$  20-inch SPS and  $R^{a(\phi=1)}$  with  $\sim 100,000$  1-inch SPS, denoted as  $C_{a(\phi=1)}^{m(\phi=20)}$ .
- IV:**  $R^{m(\phi=8)}$  with  $\sim 100,000$  8-inch SPS and  $R^{a(\phi=1)}$  with  $\sim 100,000$  1-inch SPS, denoted as  $C_{a(\phi=1)}^{m(\phi=8)}$ .

In the above configurations, the total light level of  $R^{m(\phi=20)}$ ,  $R^{m(\phi=8)}$  are  $\sim 1500$   $n_{pd}$  per MeV, while  $R^{a(\phi=3)}$  and  $R^{a(\phi=1)}$  are  $\sim 100$  and  $\sim 25$   $n_{pd}$  per MeV respectively.

For each dual-calorimetry configuration, a calibration campaign is simulated with the following steps:

- 1.) A tunable light source (laser or led) is simulated at the detector centre with the intensity varying from MeV to GeV. Each SPS of  $R^m$  can be equally illuminated, covering its full dynamic range of interest, while each SPS of  $R^a$  remains in PCR. It is worth pointing out that radioactive sources may also help investigate the delicate NL(q) effect due to particle-dependent liquid scintillator time properties [72].
- 2.) Through comparing the responses of  $R^m$  and  $R^a$ , the  $\alpha_{NL(q)}^m$  can be extracted for each channel with the help of the linear reference response of  $R^a$  in PCR ( i.e.  $\alpha_{NL(q)}^a \rightarrow 1$  ), corresponding to Equation 8 and 9, also as shown in Figure 3.a.
- 3.) Given the extracted  $\alpha_{NL(q)}^m$ , corrections can be directly implemented on each channel and/or be performed through tuning the charge reconstruction of  $R^m$  if allowed.

Figure 3 illustrates the above steps, referred to as *channel-wise dual-calorimetry calibration*, and the considered numerical input deviation  $\alpha_{NL(q)}^m$  is hypothetical for academic illustration but can be considered to be conservative to possibly cover various kinds of realistic  $\alpha_{NL(q)}^m$  forms. Given that, the power of the dual calorimetry calibration can be quantified by reducing the original channel-wise  $\alpha_{NL(q)}^m$  by one order of magnitude to permille level.

Furthermore, in terms of event-wise energy, as shown in Figure 4.a, in parity of conditions, the  $R^{m(\phi=20)}$  is

more severely affected by the  $\alpha_{NL(q)}^m$  than the  $R^{m(\phi=8)}$ . For events uniformly distributed in the detection volume,  $R^{m(\phi=20)}$  undergoes  $\sim 1\%$  event-wise NL(q) effect, while  $\sim 0.3\%$  for  $R^{m(\phi=8)}$ . For a typical energy of 5 MeV, the native  $R^{m(\phi=20)}$  and  $R^{m(\phi=8)}$  energy responses would suffer respectively  $\sim 2\%$  and  $\sim 0.5\%$  fake energy non-uniformity induced by NL(q) before the dual-calorimetry calibration. Those are out of control within the single-calorimetry framework due to typically limited calibration sources and deployments.

With dual calorimetry calibration, the channel-wise  $\alpha_{NL(q)}^m$  is disentangled and hence corrected, leading to  $\sim 0.1\%$  control in terms of event-wise energy, as shown in Figure 4.b.I; therefore the event-wise  $\alpha_{NL(L)}^m$  can be measured independently, e.g. in the detector centre. Once  $\alpha_{NL}^m$  becomes fully known and is therefore corrected, it ensures that the  $\alpha_{NU}^m$  is extracted without any NL faked bias due to unaccounted correlations, as shown in Figure 4.b.II. Thus, this channel-wise dual-calorimetry exercise demonstrates how a more orthog-

onal calorimetric response basis can be derived and regained in the context of a more stringent energy control precision without having to account for unknown correlations.

In addition, as shown in Figure 4.a.III, the response bias due to  $\alpha_{NL(q)}^m$  could lead to a sizeable energy resolution deterioration. Again, this can be corrected by potentially up to one order of magnitude to ensure the aimed permille precision upon the channel-wise dual-calorimetry calibration, as shown in Figure 4.b.III. This performance is most impressive if one considers how much extra light would be needed to compensate for the resolution deterioration stochastically. However, this is a regime historically never attained by LSDs so far.

Beyond the channel-wise approach, the dual-calorimetry also works distribution-wise, i.e. the combination of all channels over numerous events. This is illustrated, for instance, by using cosmogenic generated signals, such as the beta decay spectrum of  $^{12}\text{B}$  isotope, typically generated upon cosmic-muon spallation on  $^{12}\text{C}$

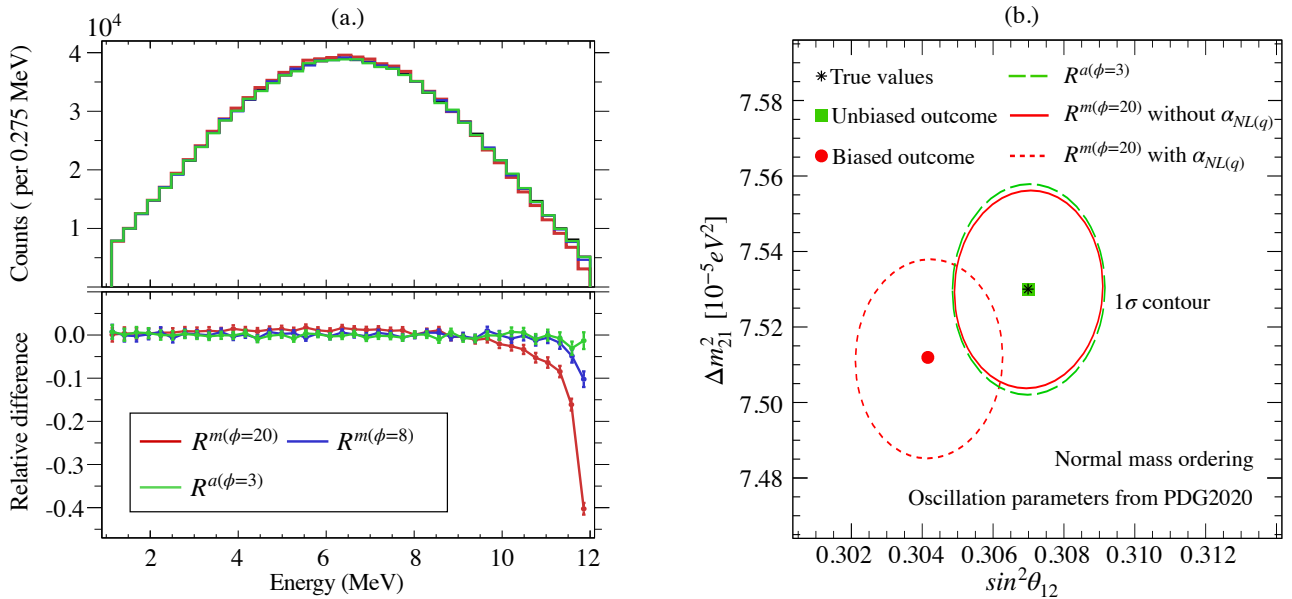


Figure 5: **(a.) Distribution-wise Dual-Calorimetry Demonstration with  $^{12}\text{B}$  Spectrum.** Under dual-calorimetry configuration, the cosmogenic-generated  $^{12}\text{B}$  spectrum can be measured by the PIR calorimetry indicated by the red and blue histograms in the top panel for  $R^{m(\phi=20)}$  and  $R^{m(\phi=8)}$  respectively; it can also be measured with the PCR calorimetry indicated by the green histogram for  $R^{a(\phi=3)}$  (or  $R^{a(\phi=1)}$ ). The impact of NL(q) introduced in Figure 3.a distorts the measured  $^{12}\text{B}$  spectrum when using PIR, as opposed to the robust PCR measurement, which can serve as a reference spectrum. The measured spectrum is compared with the true spectrum (unbiased), with the relative difference shown in the bottom panel. **(b.) Dual-Calorimetry with Oscillation Parameters  $\theta_{12}$  and  $\Delta m_{21}^2$ .** For the dual-calorimetry in a JUNO-like experimental configuration [8], the oscillation parameters  $\theta_{12}$  and  $\Delta m_{21}^2$  can be measured through reactor neutrinos by both PIR calorimetry and PCR calorimetry. Under  $C_{a(\phi=3)}^m$  configuration, the  $R^{m(\phi=20)}$  system has  $\sim 3\%/\sqrt{E}$  resolution, while  $R^{a(\phi=3)}$  has  $\sim 12\%/\sqrt{E}$  resolution. Both systems can extract  $\theta_{12}$  and  $\Delta m_{21}^2$  with comparable precision (indicated by the  $1\sigma$  contours) from exactly the same data sample which, in this case, contains  $\sim 100$  thousand events. For  $R^{a(\phi=3)}$  with robust linear response, the extracted physics parameters are unbiased (green point) in comparison with the true values (black point). For  $R^{m(\phi=20)}$ , the introduced bias in energy as described in Figure 4.a.I will bias the extracted physics parameters, as indicated by the red point. Therefore, the NL(q) induced bias in  $R^{m(\phi=20)}$  can be diagnosed given the robust  $\theta_{12}$  and  $\Delta m_{21}^2$  measurement with  $R^{a(\phi=3)}$ . The statistic uncertainty and reactor-related uncertainty [69] are considered.

readily found in LSDs. The main and auxiliary systems provide independent estimations on the same event sampling across the full detector volume and energy range of interest. Hence, the distribution-wise approach enables the extraction of the overall  $\alpha_{NL(q)}^m$  information, as illustrated in Figure 5.a. This grants quantitative insight into the residual effects of the channel-wise approach after calibration for its persistent monitoring.

The advantages of the dual-calorimetry can go beyond the calibration context, as it may enable a unique framework for testing the energy response impact of the measurement of physics parameters. This implies that the systematics of physics parameters can be diagnosed and quantified with extreme sensitivity relative to subtle detector response biases. To illustrate this point, Figure 5.b shows the potential accuracy of the measurement of neutrino oscillation parameters  $\theta_{12}$  and  $\Delta m_{12}^2$ , as obtained by dual-calorimetry systems in a JUNO-like experimental configuration.

Yet another advantage of the dual-calorimetry design enables an effective extension over the dynamic range of the overall detector. The use of smaller SPS by the auxiliary photonics system allows the measurement of light at higher energies even when the main photonics system turns limited by typical readout saturation effects. This feature has been preliminarily exploited for cosmic-muon [73], tagging the generation of cosmogenic isotopes, and even proton decay discovery searches [74].

## The Optimal Calorimetry Strategy

The presented multi-calorimetry detector discussion – single versus dual calorimetry – exploiting the advantages of different photonics interfaces working in PCR, PIR or both, raises the question of whether there is an optimal – or ultimate – detector design to yield the highest possible calorimetry precision with the simplest photonics interface. The main limitation of addressing this tempting question is the large amount of detector-specific elements leading to non-negligible compromises for any final design. In fact, the dual-calorimetry can be regarded as one such compromise, where a minimal detector evolution enables a much-increased performance while maintaining, as a priority, the dominant cost-effectiveness of the PIR single-calorimetry design.

However, while ignoring some of those compromises, it is possible that the aforementioned hypothetical dual-calorimetry designs could have been substituted by a detector with a single photonics interface using 3-inch or even 1-inch photo-sensors. Such a detector would work in a strict PCR, thus benefiting from the immunity of charge measurement effects and enabling the simplifica-

tion of the readout electronics, such as a discriminator digital system, for a lower bandwidth to maximise cost-effectiveness. The energy estimator is no longer analogue but digital, leading to minimal calorimetry systematics.

It is worth noting that the full digital readout may have non-negligible challenges at higher energies due to higher channel multiplicity. The expected non-linearity due to Poissonian multiplicity saturation can be corrected accurately, providing that not all channels are hit at once [38]. Such saturation effects may be further mitigated by reducing the photo-sensor dimensions, shortening the digitisation time unit or adding charge digitisation capability as redundancy.

So, a low-cost digital single-calorimetry detector, thus working in deep PCR, is an attractive possible optimal detector design candidate solution in terms of energy control over the largest possible energy range, but it also holds several other ideal features worth mentioning. Smaller photo-sensors are known to benefit from much better resolution for vertex reconstruction resolution due to their much better timing and effectively negligible dimensions. Also, smaller photo-sensors are far more implosion resilient, as opposed to larger photo-sensors [75, 76], thus reducing design overheads.

In other words, the dual-calorimetry can be considered as an effective optimal PCR-based detector, given that the PIR can be calibrated with PCR by using synergies, as demonstrated before. Considering the optimal calorimetry detector design, it may indirectly address another interesting question, that is, whether the dual-calorimetry concept could be further generalised towards more than two photonics interfaces. Generally, increasing *multi-calorimetry* beyond the dual-calorimetry concept cannot be ruled out a priori. Because it becomes more and more common that neutrino detectors turn into effective multi-physics observatories, addressing simultaneously fundamental particle physics, astrophysics and beyond. It implies one detector targeting simultaneously different energy ranges with high precision. Even though a dual calorimetry condition can be fulfilled for a certain energy range, it can be violated beyond that range. Hence, additional photonics interface may be helpful to reach the PCR condition, while this should be led by specific experiment conditions

## Conclusions

Much of the history of neutrino detection and physics is linked to advances in their photonics technology and techniques for controlling the ultimate precision of observables, where energy measurement is most critical.

Most neutrino experiments so far have relied on single-calorimetry designs (even not called so), while for the future LSD the extreme control in energy pushes the traditional single-calorimetry boundaries beyond. The dual-calorimetry design is hereby described in full for the first time, targeting high-precision energy detection systematics control over any vast dynamic range. The main rationale is to endow the detector calorimetry with multiple synergic photonics interfaces, thus leading to the breakdown of calorimetric response correlations. Therefore, the simplest and most precise energy definition can be achieved robustly. In this framework, the design of the combined calibration scheme is critical for the optimisation and full exploitation of the dual-calorimetry technique. The future of advances in light-based neutrino detectors remains tightly bound to advances in photonics technology and techniques, where the dual-calorimetry is a novel design candidate in addition to full PCR calorimetry for the optimal calorimetry design.

## Acknowledgement

Anatael Cabrera acknowledges the key contributions of Yosuke Abe (PhD thesis), under close supervision by Masaki Ishitsuka and Masahiro Kuze, in the original developments of the so-called “ $\alpha$  calibration” for the Double Chooz experiment in tight collaboration between the APC (Paris, France) and Tokyo Institute of Technology (Tokyo, Japan). Yang Han acknowledges the support of the National Natural Science Foundation of China with Grant No.12205391 and the Natural Science Foundation of Guangdong Province with Grant No.2023A1515012045.

## References

- [1] F. Reines and M. L. Perl. The nobel prize in physics 1995. [www.nobelprize.org/prizes/physics/1995/summary](http://www.nobelprize.org/prizes/physics/1995/summary).
- [2] R. Davis Jr. and M. Koshiba. The nobel prize in physics 2002. [www.nobelprize.org/prizes/physics/2002/summary](http://www.nobelprize.org/prizes/physics/2002/summary).
- [3] T. Kajita and A. B. McDonald. The nobel prize in physics 2015. [www.nobelprize.org/prizes/physics/2015/summary](http://www.nobelprize.org/prizes/physics/2015/summary).
- [4] B. K. Lubshandorzhiev. On the history of photomultiplier tube invention. *NIMA*, 567(1):236–238, nov 2006.
- [5] J. B. Birks. *The Theory and Practice of Scintillation Counting*. Elsevier, 1964.
- [6] P. A. Cherenkov. Visible luminescence of pure liquids under the influence of  $\gamma$ -radiation. *Dokl. Akad. Nauk SSSR*, 2(8):451–454, 1934.
- [7] P. A. Cerenkov. Visible radiation produced by electrons moving in a medium with velocities exceeding that of light. *Phys. Rev.*, 52:378–379, 1937.
- [8] JUNO Collaboration. JUNO physics and detector. *Prog. Part. Nucl. Phys.*, 123:103927, 2022.
- [9] H. Sekiya. Low energy neutrinos in superkamiokande. *Journal of Physics: Conference Series*, 718(6):062052, may 2016.
- [10] SNO Collaboration. Low-energy-threshold analysis of the phase i and phase ii data sets of the sudbury neutrino observatory. *Phys. Rev. C*, 81:055504, May 2010.
- [11] C. L. Cowan et al. Detection of the free neutrino: A Confirmation. *Science*, 124:103–104, 1956.
- [12] M. Apollonio et al. Limits on neutrino oscillations from the CHOOZ experiment. *Phys. Lett. B*, 466:415–430, 1999.
- [13] F. Boehm et al. Search for neutrino oscillations at the Palo Verde nuclear reactors. *Phys. Rev. Lett.*, 84:3764–3767, 2000.
- [14] KamLAND Collaboration. First results from KamLAND: Evidence for reactor anti-neutrino disappearance. *Phys. Rev. Lett.*, 90:021802, 2003.
- [15] C. Athanassopoulos et al. Evidence for anti-muon-neutrino to anti-electron-neutrino oscillations from the LSND experiment at LAMPF. *Phys. Rev. Lett.*, 77:3082–3085, 1996.
- [16] B. Armbruster et al. Upper limits for neutrino oscillations muon-anti-neutrino to electron-anti-neutrino from muon decay at rest. *Phys. Rev. D*, 65:112001, 2002.
- [17] T. Araki et al. Experimental investigation of geologically produced antineutrinos with KamLAND. *Nature*, 436:499–503, 2005.
- [18] Daya Bay Collaboration. Observation of electron-antineutrino disappearance at Daya Bay. *Phys. Rev. Lett.*, 108:171803, 2012.
- [19] Double Chooz Collaboration. Indication of Reactor  $\bar{\nu}_e$  Disappearance in the Double Chooz Experiment. *Phys. Rev. Lett.*, 108:131801, 2012.

- [20] RENO Collaboration. Observation of Reactor Electron Antineutrino Disappearance in the RENO Experiment. *Phys. Rev. Lett.*, 108:191802, 2012.
- [21] Borexino Collaboration. Direct Measurement of the Be-7 Solar Neutrino Flux with 192 Days of Borexino Data. *Phys. Rev. Lett.*, 101:091302, 2008.
- [22] Borexino Collaboration. Measurement of the solar 8B neutrino rate with a liquid scintillator target and 3 MeV energy threshold in the Borexino detector. *Phys. Rev. D*, 82:033006, 2010.
- [23] Borexino Collaboration. First evidence of pep solar neutrinos by direct detection in Borexino. *Phys. Rev. Lett.*, 108:051302, 2012.
- [24] Borexino Collaboration. Comprehensive measurement of  $pp$ -chain solar neutrinos. *Nature*, 562(7728):505–510, 2018.
- [25] Borexino Collaboration. Experimental evidence of neutrinos produced in the CNO fusion cycle in the Sun. *Nature*, 587:577–582, 2020.
- [26] KamLAND-Zen Collaboration. Search for the Majorana Nature of Neutrinos in the Inverted Mass Ordering Region with KamLAND-Zen. *Phys. Rev. Lett.*, 130(5):051801, 2023.
- [27] SNO+ Collaboration. The SNO+ experiment. *JINST*, 16(08):P08059, 2021.
- [28] Super-Kamiokande Collaboration. Evidence for oscillation of atmospheric neutrinos. *Phys. Rev. Lett.*, 81:1562–1567, 1998.
- [29] SNO Collaboration. Direct evidence for neutrino flavor transformation from neutral current interactions in the Sudbury Neutrino Observatory. *Phys. Rev. Lett.*, 89:011301, 2002.
- [30] K. Hirata et al. Observation of a Neutrino Burst from the Supernova SN 1987a. *Phys. Rev. Lett.*, 58:1490–1493, 1987.
- [31] R. M. Bionta et al. Observation of a Neutrino Burst in Coincidence with Supernova SN 1987a in the Large Magellanic Cloud. *Phys. Rev. Lett.*, 58:1494, 1987.
- [32] Hyper-Kamiokande Collaboration. Hyper-Kamiokande Design Report, arXiv:1805.04163 . 5 2018.
- [33] IceCube Collaboration. The IceCube Neutrino Observatory: Instrumentation and Online Systems. *JINST*, 12(03):P03012, 2017.
- [34] KM3Net Collaboration. Letter of intent for KM3NeT 2.0. *J. Phys. G*, 43(8):084001, 2016.
- [35] BAIKAL Collaboration. Deep-Underwater Cherenkov Detector in Lake Baikal. *J. Exp. Theor. Phys.*, 134(4):399–416, 2022.
- [36] A. Cabrera. High precision calorimetry with liquid scintillator detectors, <https://doi.org/10.5281/zenodo.8268175>, March 2016.
- [37] A. Cabrera. Juno stereo-calorimetry, <https://doi.org/10.5281/zenodo.1314425>, July 2018.
- [38] E. Chauveau. Calibration and energy scale in double chooz, <https://doi.org/10.5281/zenodo.1314380>, June 2018.
- [39] CUPID Collaboration. CUPID pre-CDR. 7 2019.
- [40] nEXO Collaboration. nEXO Pre-Conceptual Design Report. 5 2018.
- [41] Borexino Collaboration. Simultaneous precision spectroscopy of  $pp$ ,  ${}^7\text{Be}$ , and  $pep$  solar neutrinos with borexino phase-ii. *Phys. Rev. D*, 100:082004, Oct 2019.
- [42] A. Cabrera et al. Neutrino Physics with an Opaque Detector. *Commun. Phys.*, 4:273, 2021.
- [43] D. S. Ayres et al. NOvA: Proposal to Build a 30 Kiloton Off-Axis Detector to Study  $\nu_\mu \rightarrow \nu_e$  Oscillations in the NuMI Beamline, arXiv:hep-ex/0503053. 3 2004.
- [44] MINOS Collaboration. The Magnetized steel and scintillator calorimeters of the MINOS experiment. *Nucl. Instrum. Meth. A*, 596:190–228, 2008.
- [45] T2K Collaboration. T2K ND280 Upgrade - Technical Design Report, arXiv:1901.03750. 1 2019.
- [46] SoLid Collaboration. SoLid: a short baseline reactor neutrino experiment. *JINST*, 16(02):P02025, 2021.
- [47] I. Alekseev et al. Search for sterile neutrinos at the danss experiment. *Physics Letters B*, 787:56–63, 2018.
- [48] Borexino Collaboration. Correlated and integrated directionality for sub-MeV solar neutrinos in Borexino. *Phys. Rev. D*, 105(5):052002, 2022.
- [49] SNO+ Collaboration. Evidence of Antineutrinos from Distant Reactors using Pure Water at SNO+. *Phys. Rev. Lett.*, 130(9):091801, 2023.

- [50] J. R. Alonso et al. Advanced Scintillator Detector Concept (ASDC): A Concept Paper on the Physics Potential of Water-Based Liquid Scintillator. 9 2014.
- [51] M. Yeh et al. A new water-based liquid scintillator and potential applications. *Nucl. Instrum. Meth. A*, 660:51–56, 2011.
- [52] M. Askins et al. THEIA: an advanced optical neutrino detector. *Eur. Phys. J. C*, 80(5):416, 2020.
- [53] S. D. Biller et al. Slow fluors for effective separation of Cherenkov light in liquid scintillators. *Nucl. Instrum. Meth. A*, 972:164106, 2020.
- [54] Z. Y. Guo et al. Slow Liquid Scintillator Candidates for MeV-scale Neutrino Experiments. *Astropart. Phys.*, 109:33–40, 2019.
- [55] Wikipedia. Flash adc — Wikipedia, the free encyclopedia, 2023. [Online; accessed 15-July-2023].
- [56] G.M. Haller and B.A. Wooley. An analog memory integrated circuit for waveform sampling up to 900 mhz. *IEEE Transactions on Nuclear Science*, 41(4):1203–1207, 1994.
- [57] Double Chooz Collaboration. The Double Chooz antineutrino detectors. *Eur. Phys. J. C*, 82(9):804, 2022.
- [58] Borexino Collaboration. The Borexino detector at the Laboratori Nazionali del Gran Sasso. *Nucl. Instrum. Meth. A*, 600:568–593, 2009.
- [59] R. Gioacchino and others. Pulse-shape discrimination of liquid scintillators. *Nucl. Instrum. Meth. A*, 412(2):374–386, 1998.
- [60] Double Chooz Collaboration. Ortho-positronium observation in the Double Chooz Experiment. *JHEP*, 10:032, 2014.
- [61] Daya Bay Collaboration. A high precision calibration of the nonlinear energy response at Daya Bay. *Nucl. Instrum. Meth. A*, 940:230–242, 2019.
- [62] Double Chooz Collaboration. Double Chooz  $\theta_{13}$  measurement via total neutron capture detection. *Nature Phys.*, 16(5):558–564, 2020.
- [63] JUNO Collaboration. Calibration Strategy of the JUNO Experiment. *JHEP*, 03:004, 2021.
- [64] Zhang Fei-Hong et al. Measurement of the liquid scintillator nonlinear energy response to electron. *Chinese Physics C*, 39(1):016003, jan 2015.
- [65] F. Ardellier et al. Letter of intent for Double-CHOOZ: A Search for the mixing angle  $\theta_{13}$ , arXiv:hep-ex/0405032. 5 2004.
- [66] Daya Bay Collaboration. The Detector System of The Daya Bay Reactor Neutrino Experiment. *Nucl. Instrum. Meth. A*, 811:133–161, 2016.
- [67] J. K. Ahn et al. RENO: An Experiment for Neutrino Oscillation Parameter  $\theta_{13}$  Using Reactor Neutrinos at Yonggwang, arXiv:1003.1391. 3 2010.
- [68] Y. Han. Phd thesis: Dual calorimetry for high precision neutrino oscillation measurement at juno experiment. *tel-03295420*, 2020.
- [69] JUNO Collaboration. Sub-percent precision measurement of neutrino oscillation parameters with JUNO. *Chin. Phys. C*, 46(12):123001, 2022.
- [70] Hamamatsu. [www.hamamatsu.com/us/en/why-hamamatsu/20inch-pmts](http://www.hamamatsu.com/us/en/why-hamamatsu/20inch-pmts).
- [71] North Night Vision Technology. <http://bfys.norincogroup.com.cn/>.
- [72] X.L. Li et al. Timing properties and pulse shape discrimination of LAB-based liquid scintillator. *Chinese Physics C*, 35(11):1026–1032, 2011.
- [73] C. Genster et al. Muon reconstruction with a geometrical model in JUNO. *JINST*, 13(03):T03003, 2018.
- [74] JUNO Collaboration. JUNO Sensitivity on Proton Decay  $p \rightarrow \bar{\nu}K^+$  Searches, arXiv:2212.08502. 12 2022.
- [75] D. Milind and et al. Underwater implosions of large format photo-multiplier tubes. *NIMA*, 670:61–67, 2012.
- [76] J.J. Ling et al. Implosion chain reaction mitigation in underwater assemblies of photomultiplier tubes. *NIMA*, 729:491–499, 2013.